Original Article

Numerical modelling and experimental validation of the effect of ultrasonic melt treatment in a direct-chill cast AA6008 alloy billet

Tungky Subroto [a,*], Gerard S.B. Lebon [a,b], Dmitry G. Eskin [a,c], Ivan Skalicky [d], Dan Roberts [d], Iakovos Tzanakis [e,f], Koulis Pericleous [b]

[a] Brunel Centre for Advanced Solidification Technology (BCAST), Brunel University London, Uxbridge, UB8 3PH, UK
[b] Computational Science and Engineering Group, University of Greenwich, 30 Park Row, London, SE10 9LS, UK
[c] Tomsk State University, Tomsk, 634050, Russia
[d] Constellium UTC, Brunel University London, Uxbridge, UB8 3PH, UK
[e] Faculty of Technology, Design and Environment, Oxford Brookes University, Oxford, OX33 1HX, UK
[f] Department of Materials, University of Oxford, Oxford, OX1 3PH, UK

ARTICLE INFO

ABSTRACT

In this work, we study how ultrasonic cavitation melt treatment (UST) affects the temperature distribution, sump profile, and resulting microstructure in the direct-chill (DC) casting of an AA6008 aluminum alloy. Two 152 mm diameter billets were cast; one was treated with UST (UST-DC casting) in the hot top while the other was not (conventional DC casting). To investigate the temperature distribution, temperature was measured at multiple points in both billets. The sump profile was visualized by pouring Zn into the sump during casting. The microstructure was analyzed by measuring the grain size of as-cast billets. A numerical model of DC casting and UST-DC casting has been validated with the temperature measurements across the billets, and the experimental results agrees well with the numerical model. It is found that the sump profile quantification with thermocouple measurements is more accurate and less prone to interpretation than with Zn tracing. Numerical simulation results show that UST application in the hot top with sonotrode position at 20 mm above the graphite ring level depresses the liquidus isotherm but does not affect the solidus isotherm, resulting in a thinner transition region compared with conventional DC casting. Grain structure analysis verifies that structure refinement with UST has been achieved at the given sonotrode position. The strongest grain refinement was at the center of the billet with the average grain size 50% smaller than that without UST. The results are discussed in terms of the known mechanisms of UST, i.e. dendrite fragmentation and deagglomeration of nucleating substrates.

---

* Corresponding author.
E-mail addresses: Tungky.subroto@brunel.ac.uk, tungky.subroto@gmail.com (T. Subroto).

1. Introduction

Direct-chill (DC) casting is a semi-continuous casting process that is widely used in the non-ferrous metallurgical industry. It is robust in producing commercial wrought aluminum alloy billets that are suitable for further rolling, extrusion, or remelting processes [1,2]. To avoid casting defects and improve the thermo-mechanical properties of the as-cast billet, a finer grain structure is usually necessary. Finer grained alloys display superior mechanical characteristics such as strength, toughness, and ductility [3]; these properties are crucial for technological applications.

The European Metallurgical Roadmap of 2050 demands better mechanical performance of aluminum alloys [4]. Refining the microstructure with grain refining chemicals is one of the established routes towards this aim [5–7]. Established techniques involve inoculants that are costly and whose production involves hazardous chemicals and processes [8]. External field techniques, including ultrasonic melt treatment (UST) technology, are attractive alternative methods to treat light alloys [9–12]. UST has gained popularity as a more economical and environmentally friendly alternative as it enables the refining of the cast product structure with significantly less — or even without — inoculants.

Eskin and Eskin [8] have methodically assessed the mechanisms of structure refinement using UST of light alloys. These mechanisms are:

1. Enhanced heterogeneous nucleation of primary phases by activating non-metallic inclusions, such as oxides by wetting [13].
2. Fragmentation of primary intermetallics that provide substrates on which Al grains can nucleate [14,15].
3. Fragmentation of aluminum dendrites [16].

These mechanisms strictly rely on the main actor of UST: acoustic cavitation (pressure bubbles). Acoustic bubbles form when the sonotrode vibrates at an ultrasonic frequency in the melt generating alternating high- and low-pressure fields. Bubbles vigorously oscillate and ultimately collapse, releasing pressure shockwaves that produce local pressure spikes in the range of 0.4–1 GPa [17] and a temperature jump of up to $2 \times 10^4 \,^\circ$C [18]. These spikes can activate latent inclusions in the melt and fragment suspended solid structures — intermetallics and Al-dendrites — near the collapse [14].

The oscillating sonotrode also generates a macroscopic flow, acoustic streaming, which has a vortex-like recirculation pattern. The liquid stream is pushed away from the sonotrode, disperses, and then recirculates back into the main streamer [19]. Acoustic streaming extends the UST effects to the larger melt volume by transporting cavitation bubbles to the bulk liquid and bringing fresh melt into the cavitation region [20]. Acoustic streaming also reduces the temperature gradient across the melt volume and promotes the desirable equiaxed grain structure formation [21]. Furthermore, streaming uniformly disperses and distributes nanoparticles deagglomerated by cavitation, thus improving the resulting microstructure in metal-matrix-nano-composite alloys [22,23].

In DC casting, UST is typically performed in the hot top or billet sump [8,24]. A previous study showed that structure refinement depends on the distance between the sonotrode tip and the solidification front [25]. Previous studies have also demonstrated that forced convection near the solidification front influences the sump profile [26,27], and ultimately affects the billet quality. If the sonotrode is too far from the liquidus isosurface, the UST effect is suboptimal. Conversely, strong acoustic streaming modifies the shape of the sump: this may be undesirable because it can promote solidification defects such as hot tearing or porosity [21]. Therefore, the immersion height of the sonotrode tip in the DC casting hot top needs to be optimized for different process conditions and alloys, because the sump profile differs in each case [28,29] and the thickness of the transition zone varies with different chemical compositions and grain refiners [3].

Traditionally, the optimum process conditions in DC casting have been obtained heuristically, but these haphazard searches are inefficient from both time and resource considerations. Numerical modelling is a powerful tool that can assist in locating the optimum process parameters in the DC casting of aluminum alloys [28,29]. For example, a DC casting model that was developed by Lebon et al. [30], based on the continuum model of Bennon and Incropera [31], showed how the sump was modified and how heat transfer was enhanced by forced convection from the high-shear rotor-stator mixer.

Acoustic cavitation is a complex, non-linear, and multi-scale phenomenon. Although there exist several numerical models that capture acoustic pressure in UST [32–35], only few include the four critical phenomena of UST in the melt: acoustic streaming, acoustic pressure, cavitation, and solidification. Peng et al. [36] applied an ultrasonic treatment model in a DC casting simulation of an aluminum alloy. Although this model was developed for a DC casting process, it only considered the acoustic pressure distribution throughout the melt, without considering cavitation. Meanwhile, Komarov and Yamamoto [37] developed a more advanced model that simulated the cavitation phenomenon and acoustic pressure distribution all while considering the effect of acoustic streaming in the melt, but their model did not incorporate solidification.

Lebon et al. [38] have developed a multiscale UST model that considers the four aforementioned phenomena and applied the model to a DC casting case of aluminum alloys. This model simulated UST-DC casting with different UST parameters (i.e. power of ultrasonic transducer and sonotrode distance to solidification front). The simulation results obtained — such as the modification of sump shape due to the presence of acoustic streaming — could logically explain the grain structure modification [25]. However, the model still needs temperature profile validation from a DC casting experiment, a critical step to ascertain model's accuracy.

The thermal history of a DC casting billet is generally measured with multiple thermocouples. These measurements are used to optimize the process [39] and validate numerical models [40]. This method can be more accurate in predicting the sump shape [41], compared with the commonly used doping of denser elements into the melt during casting (e.g. addition of zinc [3] during horizontal DC casting of Mg

alloy, or Al-30 wt.% Cu in DC casting of Al-17 wt.% Si [37] and AA7050 [41]).

So far, there has been no experimental study on the effect of UST on the sump shape in DC casting. Therefore, the following questions remain unanswered: (1) What do the melt flow pattern and the temperature profile look like in the cross-section of a billet? (2) Will the melt inflow rate, that is typical in DC casting, be sufficient to maintain the axial symmetry of the sump when UST is applied to DC casting? (3) Can the numerical model of UST-DC casting accurately predict temperature distribution in the sump?

In this work, we performed multiple-thermocouple measurements across the billet to obtain the temperature at multiple points across the radii of the billet in two sections, one parallel and the other perpendicular to the melt inflow from the launder. These measurements were made in both conventional and UST-DC casting of a commercial grade aluminum alloy (AA6008) typically used for automotive applications. The temperatures were used to reconstruct the sump shape, to assess the effects of UST and inlet flow on the sump shape, and to validate the DC casting numerical model. The sump shape was observed by pouring Zn (as a tracer) into the melt during casting. The grain structure was analyzed experimentally. This study shows how UST affects the sump profile and grain structure and is a critical step towards the optimization of UST parameters in DC casting of aluminum alloys.

2. Methodology

2.1. Experimental setup

DC casting of an AA6008 alloy was performed in the Advanced Metal Casting Centre (AMCC) of the Brunel Centre of Advanced Solidification Technology (BCAST) in Brunel University London, UK. The billet had a diameter of 152 mm and was cast with a hot top of diameter 155 mm. An Al5Ti1B grain refiner was added to the melt. Two billets were cast at 140 mm min^{-1}; one billet was cast by conventional DC-casting, and the other with UST in the hot top. The melt temperature in the hot top was 674 °C for conventional DC casting and 663 °C for UST-DC casting. This temperature difference is due to the temperature control oscillation in the launder heating system and may also be due to the relatively cold (though preheated) sonotrode which is connected to a water-cooled transducer.

The experimental setup of the UST-DC casting is illustrated in Fig. 1a. UST was carried out by the water-cooled 5-kW magnetostrictive transducer (Reltec) with a driving frequency of 17.3 kHz at a working power of 3.5 kW (corresponding to a 40 μm peak-to-peak amplitude). A pre-heated conical Nb sonotrode, with a working diameter of 20 mm, delivered ultrasonic power to the melt. The sonotrode tip was approximately 20 mm above the graphite ring level.

Temperatures were continuously recorded using 5 type-K thermocouples (1.5 mm sheath diameter) with positions of each thermocouple as shown in Fig. 1b. The positions of the thermocouples were chosen to assess how three-dimensional flow, including that from the launder, affects the temperature profile across the billet. When casting reached steady state, the thermocouples were lowered simultaneously with 'anchors' that were attached slightly lower than the thermocouple tips. The anchors solidify first, thereby ensuring that the thermocouples were always lowered constantly at the casting speed. Temperatures were recorded using the National Instruments data acquisition (DAQ) systems with an effective DAQ resolution of 2 Hz. A 'Y.CT Compact XL Mag' computed tomography system (YXLON International, 450 KV, 1 mA) was used to verify the radial thermocouple tip positions
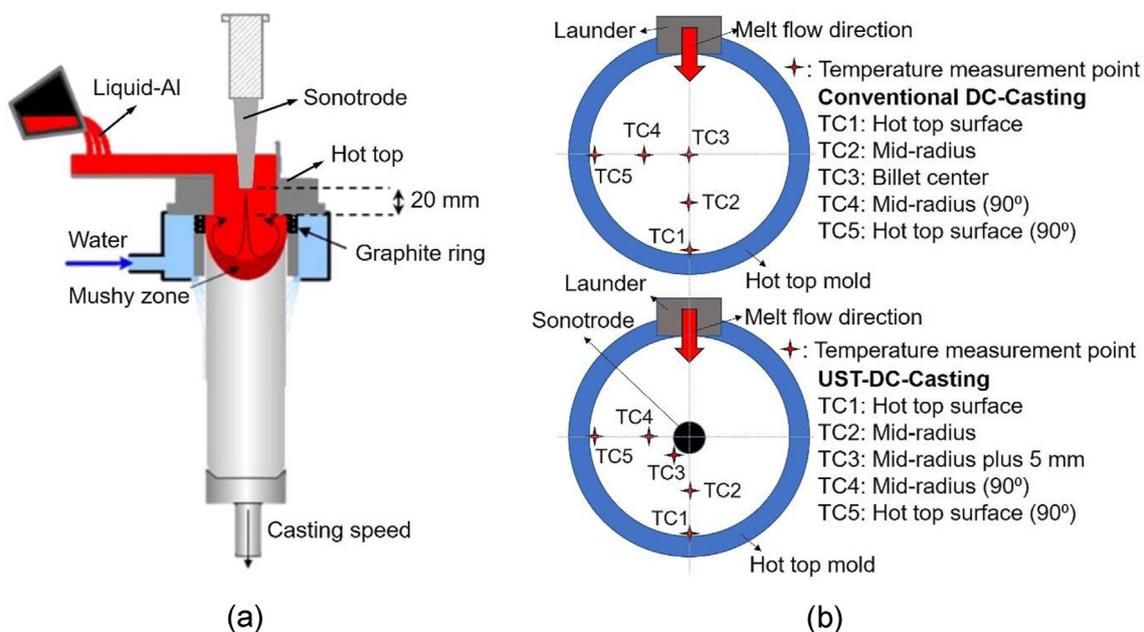
Fig. 1 − (a) Illustration of UST-DC-casting setup with ultrasonic sonotrode in the hot top (adapted from [25]), and (b) top-view of thermocouple positions across the hot top on both conventional DC-casting and UST-DC-casting.

in each billet, and the locations reflecting the readings were corrected accordingly.

To visualize the sump profiles in both charges, liquid Zn was poured into the melt pool. To enhance the contrast, the section of the billet with Zn was cut, mechanically polished, and etched using NaOH. The effect of UST on microstructure was verified by grain size analysis. For microstructure observation, samples were cut from different parts across the billet radius from the center to the surface at distances of 0 mm, 25 mm, 45 mm and 65 mm from the billet center, which are henceforth called "Center", "Middle-In", "Middle-Out", and "Surface", respectively. The samples were ground, polished, anodized in 5 wt.% HBF_4 using 20 VDC, and subsequently examined under an optical microscope with polarized light. The grain size was measured using the linear intercept method taken randomly upon optical microscope images and statistical analysis was performed.

The chemical composition of the melt taken from the furnace prior to casting was determined using Optical Emission Spectroscopy (OES). This composition is shown in Table 1. With the analyzed chemical composition, Thermo-Calc 2019b software (with the TCAL4 database [42]) was used to determine the solid fraction (f_s) and alloy characteristic temperatures during solidification: these values were used for the numerical simulation parameters given in Table 2. The Scheil–Gulliver solidification curve calculated with the composition shown in Table 1 is presented in Fig. 2.

2.2. Theoretical background and numerical simulation setup

The numerical simulation of UST upon DC casting should necessarily include acoustic streaming, cavitation, and their interaction with natural convection and temperature fields in the sump of a billet.

2.2.1. Acoustic streaming model
Designating the harmonic part of acoustic pressure p as $\Re(Pe^{i\omega t})$, the complex amplitude P is approximately given by the nonlinear Helmholtz equation [43].

$$\nabla^2 P + K^2 P = 0. \tag{1}$$

The real and imaginary parts of K^2 are given by

$$\Re(K^2) = \frac{\omega^2}{c^2} - \frac{\mathscr{A}}{|P|}, \text{ and} \tag{2}$$

$$\Im(K^2) = -\frac{\mathscr{B}}{|P|}, \tag{3}$$

respectively, where c is the speed of sound in the pure liquid, ω represents the angular frequency, and, based on Trujillo's derivation [44], the terms $\mathscr{A}$ and $\mathscr{B}$ are:

Table 2 – Model parameters for the DC casting simulation.

Parameter	Quantity
Casting velocity u_s (m s^{-1})	(0, 0, −0.00233)
Inlet temperature T_{in} (°C)	DC casting: 674
	UST-DC casting: 663
Liquidus temperature T_l (°C)	655
Solidus temperature T_s (°C)	533
Latent heat L_f (J kg^{-1})	351,540
Thermal expansion coefficient β (K^{-1})	23×10^{-6}
Mushy region momentum sink coefficient K (s^{-1})	1.522×10^7
Density ρ (kg m^{-3})	2602
Speed of sound c (m s^{-1}) (for UST-DC casting)	4600
Dynamic viscosity μ (Pa s)	10.155×10^{-4}
Gravitational constant g (m s^{-2})	(0, 0, −9.81)
Maximum Courant number	0.5

$$\mathscr{A} = -\frac{\rho\omega^2}{\pi} \int_0^{2\pi} \frac{\partial^2 \beta}{\partial \tau^2} \cos\left(\tau + \frac{\pi}{2}\right) d\tau, \tag{4}$$

$$\mathscr{B} = \frac{\rho\omega^2}{\pi} \int_0^{2\pi} \frac{\partial^2 \beta}{\partial \tau^2} \sin\left(\tau + \frac{\pi}{2}\right) d\tau, \tag{5}$$

where ρ is the pure liquid density; τ describes one period between $[0, 2\pi]$; and β is the bubble volume fraction

$$\beta = \frac{4}{3}\pi R^3 N = VN, \tag{6}$$

where $V = \frac{4}{3}\pi R^3$ is the bubble volume while R is the bubble radius. In this model, the bubble density N follows the step function

$$N = \begin{cases} N_0 & \text{if } |P| > P_B \\ 0 & \text{if } |P| \leq P_B \end{cases}, \tag{7}$$

where the Blake threshold is defined as $P_B = p_0\left[1 + \sqrt{\frac{4}{27}\frac{S^3}{1+S}}\right]$, and $S = \frac{2\sigma}{p_0 R_0}$. R_0 is the equilibrium radius of the bubble.
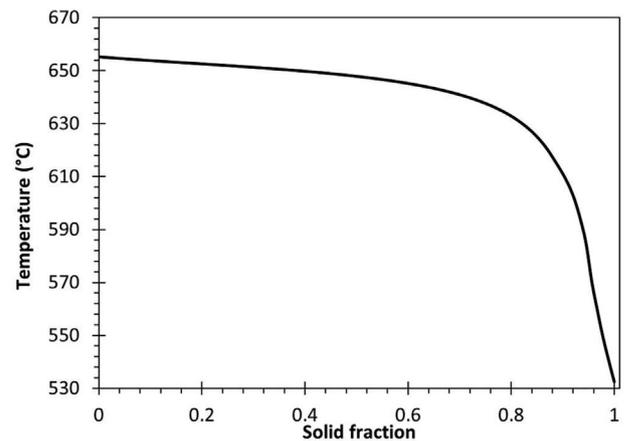
Fig. 2 – Evolution of the solid fraction according to the Scheil–Gulliver approximation based on the composition given in Table 1. The solid fraction curve was predicted in Thermo-Calc [42].

Table 1 – Chemical composition of the AA6008 alloy obtained by OES.

Al	Si	Mg	Fe	Mn	Cr	Cu	V	Zn	Ti
Bal.	0.7	0.55	0.175	0.15	0.15	0.15	0.1	0.1	0.05

Using Trujillo's method [44], $\mathscr{A}$ and $\mathscr{B}$ in Eqs. (4) and (5) are approximated from the Keller−Miksis equation:

$$\rho\left[\left(1-\frac{\dot{R}}{c}\right)R\ddot{R}+\frac{3}{2}\left(1-\frac{\dot{R}}{3c}\right)\dot{R}^2\right]=\left(1+\frac{\dot{R}}{c}+\frac{R}{c}\frac{d}{dt}\right)$$
$$\times\left[p_g+p_v-\frac{2\sigma}{R}-\frac{4\mu\dot{R}}{R}-p_0\{1-A\sin(\omega t)\}\right]. \qquad (8)$$

The surface tension between the liquid and gas phases is defined by σ, while μ is used to describe the dynamic viscosity of the liquid. p_0 is the pressure at infinity (set to atmospheric pressure), A is the pressure amplitude (normalized by p_0) of the excitation source of angular frequency ω, and p_v is the vapour pressure.

p_g (the gas pressure) is obtained from the differential equation

$$\frac{dp_g}{dt}=\frac{3}{R}\left[(\gamma-1)\left(k\frac{dT}{dr}\bigg|_{r=R}\right)-\gamma p_g\dot{R}\right], \qquad (9)$$

which considers the heat transfer effect during bubble pulsation [45,46]. k is the heat conductivity of the hydrogen gas. The gas pressure at the equilibrium radius R_0, denoted by $p_{g,0}$, is used as the initial value for equation (9). Assuming adiabatic pulsation, the polytropic exponent is $\gamma = 1.4$, the ratio of specific heats.

Following Toegel et al. [47], the temperature gradient at the bubble surface is approximated as

$$\frac{dT}{dr}\bigg|_{r=R}=\frac{T-T_\infty}{\sqrt{(RD)\big/\left\{3(\gamma-1)\dot{R}\right\}}}, \qquad (10)$$

where the gas diffusivity [45] is given by D. Liquid bulk temperature (T_∞) is taken as the inlet temperature. The first law of thermodynamics was used to estimate the temperature of the gas within the bubble (T):

$$C_v\dot{T}=4\pi R^2 k\frac{T_\infty-T}{l_{th}}-p_g\dot{V}, \qquad (11)$$

where the thermal diffusion length is defined as $l_{th} = \min\left(\frac{R}{\pi}, \sqrt{\frac{RD}{\dot{R}}}\right)$ and the specific heat capacity of the gas is given by C_v.

2.2.2. DC casting model

DC casting is modelled using a continuum formulation. The mass conservation equation is

$$\frac{\partial\rho}{\partial t}+\nabla\cdot(\rho\boldsymbol{u})=0, \qquad (12)$$

where $\boldsymbol{u}$ is the velocity of the liquid phase.

The energy conservation equation is

$$\frac{\partial(\rho h)}{\partial t}+\nabla\cdot(\rho\boldsymbol{u}h)=\nabla\cdot(\kappa\nabla T)-L_f\left[\frac{\partial(\rho f_l)}{\partial t}+\nabla\cdot(\rho\boldsymbol{u}f_l)\right], \qquad (13)$$

Table 3 − CFD equations finite-volume discretization schemes and solver control parameters [21,38].	
Discretization schemes	
Transient term discretization ($\partial/\partial t$)	Euler
Gradient terms differencing schemes (∇)	
Default method	Least squares method with cell-limited gradient
grad ($\Im(P)$), grad ($\Re(P)$) where P is the complex acoustic pressure. $\Im$ and $\Re$ denote the imaginary and real components of the complex number.	Least squares method
Divergence term differencing schemes ($\nabla\cdot$)	
Default method	Bounded Gaussian integration with linear interpolation
div (u), div (h), div (f_l), where u, h, and f_l are the velocity, enthalpy, and liquid fraction	Bounded Gaussian integration with limited linear interpolation
div (C^S) where C^S is the concentration of species S.	Bounded Gaussian integration with upwinding
Laplacian term differencing schemes ($\nabla\cdot(\Gamma\nabla)$)	
Default method	Gaussian integration with linear interpolation and explicit non-orthogonal correction
Interpolation schemes Default method	Linear interpolation
Solver control parameters	
$\Im(P)$, $\Re(P)$	Preconditioned bi-conjugate gradient (PBiCGStab) with simplified diagonal-based incomplete LU (DILU) smoother. Simplified Diagonal-based Incomplete Cholesky (DIC) preconditioner required for stability.
All other variables	Preconditioned bi-conjugate gradient (PBiCG) with simplified diagonal-based incomplete LU (DILU) preconditioner
Momentum predictor step	Yes
Number of outer correctors loops	2
Number of inner correctors loops	2
Number of energy correctors loops	7
Number of non-orthogonal correctors loops	3

where $h = C_p T$ is the enthalpy, κ is thermal conductivity, T is temperature, C_p is specific heat capacity, L_f is latent heat of fusion, and f_l is the volume fraction of liquid. The phase change is considered as the source term in equation (13) [48].

Equation (14) describes the species conservation equation

$$\frac{\partial(\rho C^s)}{\partial t} + \nabla\cdot(\rho \boldsymbol{u} C^s) = \nabla\cdot\left(\rho f_l D_l^s \nabla C^s\right) + \nabla\cdot\left\{\rho f_l D_l^s \nabla\left(C_l^s - C^s\right)\right\}$$
$$- \nabla\cdot\left\{\rho(\boldsymbol{u} - \boldsymbol{u}_s)\left(C_l^s - C^s\right)\right\}, \qquad (14)$$

where the solid shell velocity which is set as the casting speed is given by $\boldsymbol{u}_s$, while C^s is the concentration of species s, and D_l^s is the diffusivity of species s in the liquid. The lever rule is used to calculate the liquid concentration

$$C_l^s = C^s \big/ \left\{(1 - f_l)k_p + f_l\right\}, \qquad (15)$$

where k_p is a binary partition coefficient.

The transition region (between liquidus and solidus) was split into two regions: slurry (above the coherency isotherm) and mush (below the coherency isotherm) [49]. The momentum conservation equation in the liquid and slurry region ($g_c \le f_l \le 1$) is:

$$\frac{\partial(\rho \boldsymbol{u})}{\partial t} + \nabla\cdot(\rho \boldsymbol{u}\boldsymbol{u}) = \nabla\cdot(\mu \nabla \boldsymbol{u}) - \nabla p + \rho_b \boldsymbol{g} + \boldsymbol{f}, \qquad (16)$$

$$\boldsymbol{f} = -\nabla(\rho_l \overline{\boldsymbol{v} \otimes \boldsymbol{v}}), \qquad (17)$$

where the effective viscosity is defined as $\mu = \mu_t + \mu_{l,m}$, p is pressure, and $\boldsymbol{g}$ is gravity. Meanwhile, the acoustic streaming driving force represented by $\boldsymbol{f}$, g_c is the liquid fraction reflecting the coherency, and $\boldsymbol{v} = \frac{\nabla p}{\rho \omega}$ is the acoustic velocity that is obtained by solving the equation for sound propagation [50]. After acoustic velocity has been obtained, by solving equation (16), the flow velocity $\boldsymbol{u}$ can be attained. The overbar in equation (17) implies that the values are obtained from averaging over a period of the acoustic bubble.

The Boussinesq approximation is used to evaluate the buoyancy term, i.e.

$$\rho_b \boldsymbol{g} = \rho_{ref} \boldsymbol{g}\left[\beta_T(T - T_{ref}) + \sum^s \beta_s\left(C_l^s - C_0^s\right)\right], \qquad (18)$$

where the thermal expansion coefficient is described as β_T, while is the solution expansion coefficient for species s is given by β_s.

In the slurry region, to simulate flow with resistance due to the presence of the grains the viscosity is modified as following:

$$\mu_{l,m} = \mu_l \bigg/ \left\{1 - F_\mu \frac{(1 - f_l)}{A_c}\right\}^2, \qquad (19)$$

where F_μ is a switching function and A_c is a crystal constant [51].

In the mushy zone and solid regions ($0 \le f_l \le g_c$), the momentum conservation equation is given by

$$\frac{\partial(\rho \boldsymbol{u})}{\partial t} + \nabla\cdot(\rho \boldsymbol{u}\boldsymbol{u}) = \nabla\cdot(\mu \nabla \boldsymbol{u}) - \nabla p + \rho_b \boldsymbol{g} - (\boldsymbol{u} - \boldsymbol{u}_s)\frac{\left(1 - f_l^2\right)}{f_l^3}K, \qquad (20)$$

where K is the permeability coefficient.

The $k - \omega$ shear stress transport (SST) model is used for closure:

$$\frac{\partial(\rho k)}{\partial t} + \nabla\cdot(\rho \boldsymbol{u} k) = \nabla\cdot(\rho D_k \nabla k) + \rho G - \frac{2}{3}\rho k(\nabla\cdot \boldsymbol{u}) - \rho \beta^* \omega k, \qquad (21)$$

$$\frac{\partial(\rho \omega_t)}{\partial t} + \nabla\cdot(\rho \boldsymbol{u} \omega_t) = \nabla\cdot(\rho D_\omega \nabla \omega_t) + \frac{\gamma \rho G}{\nu} - \frac{2}{3}\gamma \rho \omega_t(\nabla\cdot \boldsymbol{u}) - \rho \beta_\omega \omega_t^2$$
$$- \rho(F_1 - 1)CD_{k\omega}. \qquad (22)$$

The turbulent viscosity is given by
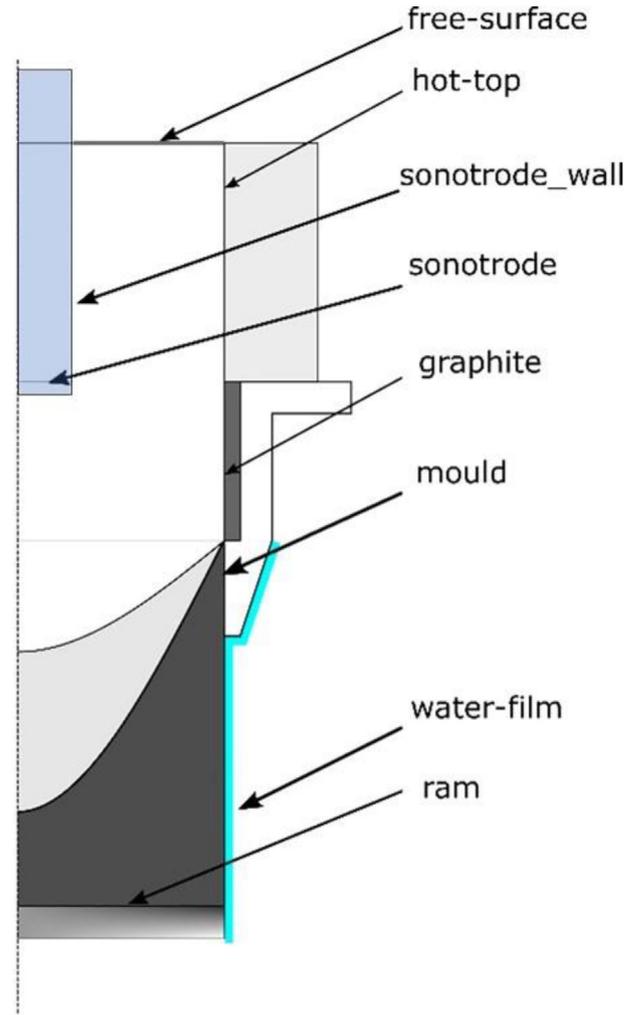
Fig. 3 – **Boundary conditions for the axis-symmetric simulation of DC casting. The bottom surface is denoted as 'ram' but does not represent an actual DC casting ram. It is instead an arbitrary section of the billet below which the simulation stops. The surface is located far below the sump so that the Neumann conditions specified in Table 4 do not affect the accuracy of the temperature simulations.**

$$\mu_{t} = a_1 \frac{\rho k}{\max(a_1 \omega_t, b_1 F_{23} \mathbf{S})}, \tag{23}$$

where the turbulence kinetic energy is given by k, and dissipation rate is defined by ω_t [52].

2.2.3. Simulation setup

The models described in Section 2.2.1 and 2.2.2 have been implemented in OpenFOAM 6 [53]. Further implementation details are found elsewhere [21,38]. In this work, 2D (axisymmetric) DC casting simulations were run to model the experiments using the simulations conditions outlined in Tables 2-4. The model parameters are described in Table 2 and the material properties contained therein were calculated from Thermo-Calc. Since the hot top temperatures differed in both experiments, the two simulations were run with their corresponding inlet temperatures. The discretization schemes and solver control parameters are described in Table 3. Suitable preconditioners are required for the acoustic pressure terms: without these, the acoustic streaming simulation would not converge. Fig. 3 and Table 4 describe the boundary conditions. The sonotrode is included only in the UST-DC casting case; for conventional DC casting, the free-surface boundary covers the whole top face. A uniform grid of size 2 mm was used in the simulations.

3. Results and discussion

We started with examining the sump profile using a widely used method of Zn outlining. The Zn penetration profiles in Fig. 4 demonstrate that the apparent sump (from the point where shell starts to solidify until the visible sump bottom) is shallower (68.5 mm) and less inclined (43°−46°) without UST (Fig. 4a) than the sump with UST-DC (Fig. 4b: 75.6 mm, 53°). In the case of UST-DC, the sump asymmetry — that could have potentially arisen due to the melt inflow from the launder — is not detected upon comparing Fig. 4b and c. Temperature measurements in the two perpendicular directions (see Fig. 5b) also do not hint at any asymmetry in the UST-DC sump profile. However, some axial asymmetry of the sump upon conventional DC casting is visible, apparently due to the effect of the inlet flow. This is shown in Fig. 4a that the sump profile angles are slightly different: 46° on left hand side and 43° on right hand side. Similar asymmetry can be observed from the temperature measurements in Fig. 5a. Apparently, the

Table 4 − Boundary conditions for the faces depicted in Fig. 3.

Velocity u	
ram	Dirichlet boundary condition with a fixed value of (0, 0, −0.00233) m s^{-1}
water-film|mould|graphite|ceramic|hot-top|sonotrode| sonotrode_wall	No slip boundary condition, i.e. $\boldsymbol{u} = 0$
free-surface	Neumann boundary condition, i.e. zero normal gradient
Pressure P	
ram	Fixed flux pressure, value 1×10^5 Pa
free-surface	Dirichlet boundary condition with a fixed value of 1×10^5 Pa
water-film|mould|graphite|ceramic|hot-top| sonotrode| sonotrode_wall	Fixed flux pressure, value 1×10^5 Pa
Temperature T	
ram	Inlet-outlet, internal value when inflow, Neumann boundary condition, i.e. zero normal gradient when outflow
free-surface	Dirichlet boundary condition with a fixed value of 674 °C for the DC casting simulation and 663 °C for the UST-DC casting simulation
hot-top| sonotrode|sonotrode_wall	Adiabatic or Neumann boundary condition, i.e. zero normal gradient
water-film|mould|graphite|ceramic	Heat transfer coefficient prescribed from a lookup table based on [54]. External temperature set to 20 °C
For UST-DC simulation only **Kinetic energy of turbulence K**	
ram	Neumann boundary condition, i.e. zero normal gradient
free-surface	Dirichlet boundary condition with a fixed value of 5.58×10^{-8} m^{2}s^{-2}
water-film|mould|graphite|ceramic|hot-top| sonotrode| sonotrode_wall	class *kqRWallFunction*, equivalent to a Neumann boundary condition, i.e. zero normal gradient [55]
Turbulent dissipation rate ω_t	
ram	Neumann boundary condition, i.e. zero normal gradient
free-surface	Dirichlet boundary condition with a fixed value of 0.001 s^{-1}
water-film|mould|graphite|ceramic|hot-top| sonotrode| sonotrode_wall	class *omegaWallFunction*, computed as sqrt (ω_vis2 + ω_log2) [55]
Real and imaginary of parts of acoustic pressure $\mathscr{R}(\mathbf{P})\|\mathfrak{I}(\mathbf{P})$	
water-film|mould|graphite|ceramic|hot-top| sonotrode_wall	Neumann boundary condition, i.e. zero normal gradient
free-surface	Dirichlet boundary condition with a fixed value of 0 Pa
Sonotrode	Dirichlet boundary condition with a fixed value of 1.6×10^7 Pa.
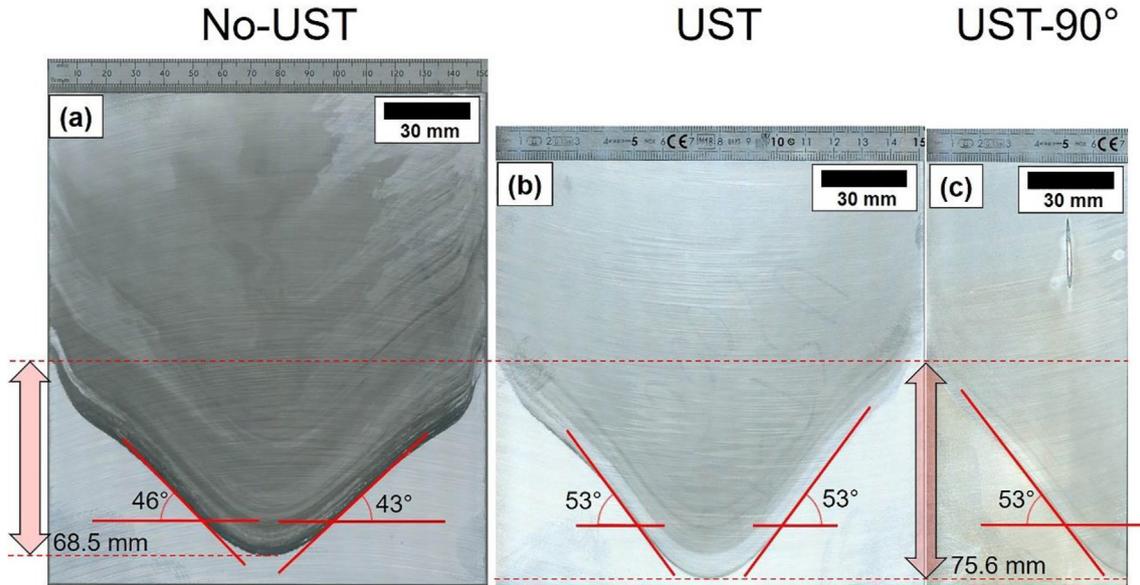
Fig. 4 – Apparent sump profiles (Zn-outlined) in the billets produced by (a) conventional DC casting and (b) UST-DC casting. (c) Shows a cross section of the UST-DC casting billet that is perpendicular to (b). The sump depth (between the dashed lines) and the inclination of the sump (solid lines) are marked.

acoustic stream in UST-DC casting accentuates symmetry of the apparent sump profile because acoustic streaming is stronger than the launder-induced flow. Based on calculations, the velocities of acoustic streaming flow and launder-induced flow (at a rate of 2.5 L min^{-1} corresponding to a casting speed of 140 mm min^{-1}) are 50 mm s^{-1} and 21 mm s^{-1}, respectively.

Although the Zn outlining gives a visual representation of the overall sump profile, the specific details depicted by this method maybe deceptive, especially when comparing the sump profiles affected by forced convection. Acoustic streaming pushes Zn deeper into the mush, a probable reason

for the lighter shade of Zn layers in Fig. 4b (UST) and Fig. 4c (UST-90°). Therefore, the deeper zinc delimitation line that is observed in UST-DC casting may not correspond to a real change in depth. Moreover, it is important to realize that Zn does not penetrate all the way to the solidus but stops at a lower fraction of solid below which the permeability is too small.

Therefore, temperature profiling using thermocouples is a preferred method when estimating measuring the sump profile [41]. Using the temperature measurements across the billet, we can reconstruct the approximate shape of the sump. Fig. 5 illustrates that the sump is actually slightly
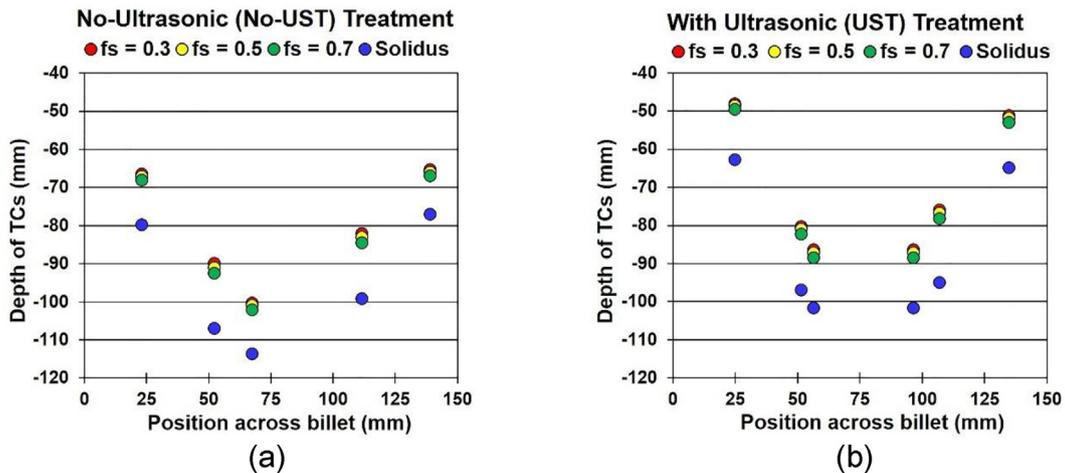
Fig. 5 – Comparison of thermocouple readings and positions at different solid fractions across the billet for (a) conventional DC casting and (b) UST-DC casting. The thermocouple position of Mid-radius + 5 mm in (b) is mirrored on both sides of billet, for the sake of illustration.
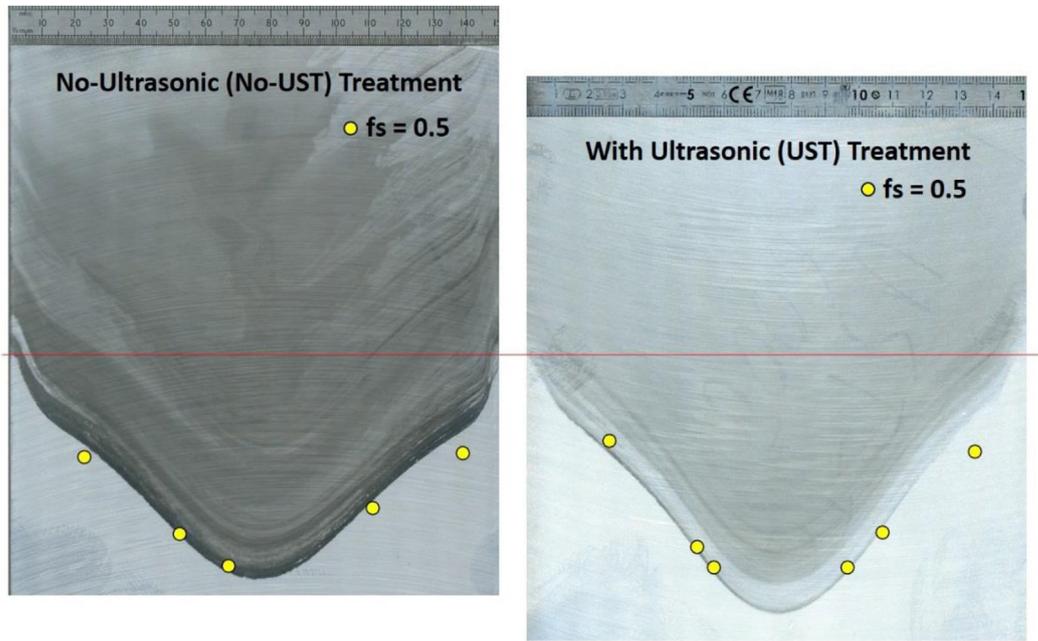
Fig. 6 − **Comparison between position of thermocouples at** $f_s = 0.5$ **and sump shape observation by Zn tracing.**

deeper in the conventional DC casting case (Fig. 5a) compared with the UST-DC casting case (Fig. 5b). In our case, the deeper sump of conventional DC casting is more logical as it results from a higher casting temperature than in the UST-DC casting case.

The uneven distance between thermocouple positions reflecting different stages of solidification (e.g. $f_s = 0.3, 0.5, 0.7$, and solidus) can be explained by the dependence of solid fraction on temperature. A Thermo-Calc calculation (Fig. 2) predicts that the temperatures corresponding to $f_s = 0.3, 0.5$, 0.7, and the solidus are 651 °C, 648 °C, 641 °C, and 533 °C,

respectively, which explains why the related measured points are close to each other at lower fractions solid as compared to higher fractions.

As suggested by Yu et al. [41], penetration of the tracer element into the mush cannot be too deep and probably stops shortly after coherency is reached and feeding becomes difficult, which may start as early as $f_s = 0.5$, thus limiting Zn penetration into the mush. Comparison between position of thermocouples at $f_s = 0.5$ and sump shape observation by Zn tracing for both conventional- and UST-DC casting is shown in Fig. 6. These figures demonstrate that the profile generated by
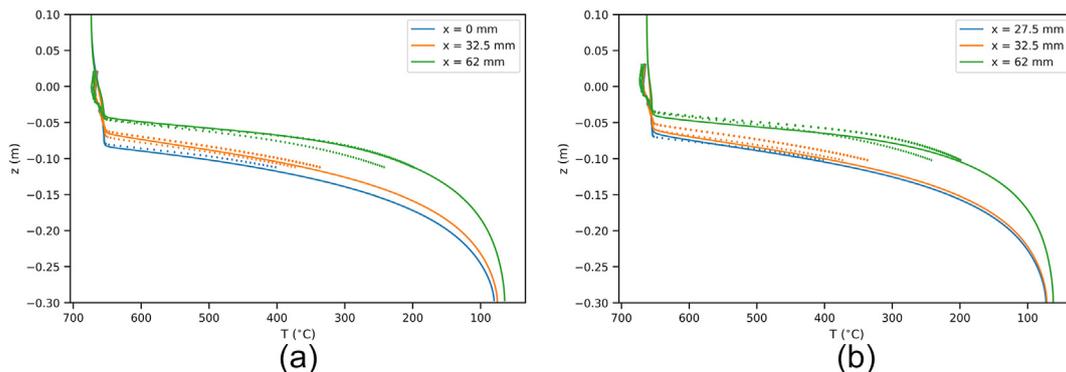
Fig. 7 − **Comparison between numerical and experimental temperature profile for (a) conventional DC-casting and (b) UST-DC casting. Thermocouple positions in the center − only for conventional DC casting (x = 0 mm), mid-radius plus 5 mm − only for USDC casting case (x = 27.5 mm), mid-radius (x = 32.5 mm) and sub-surface (x = 62 mm). Dotted line represents experimental measurements by thermocouples (two readings reflect measurements along perpendicular radii) and solid lines represent numerical simulation results.**

(a)

(b)   (c)
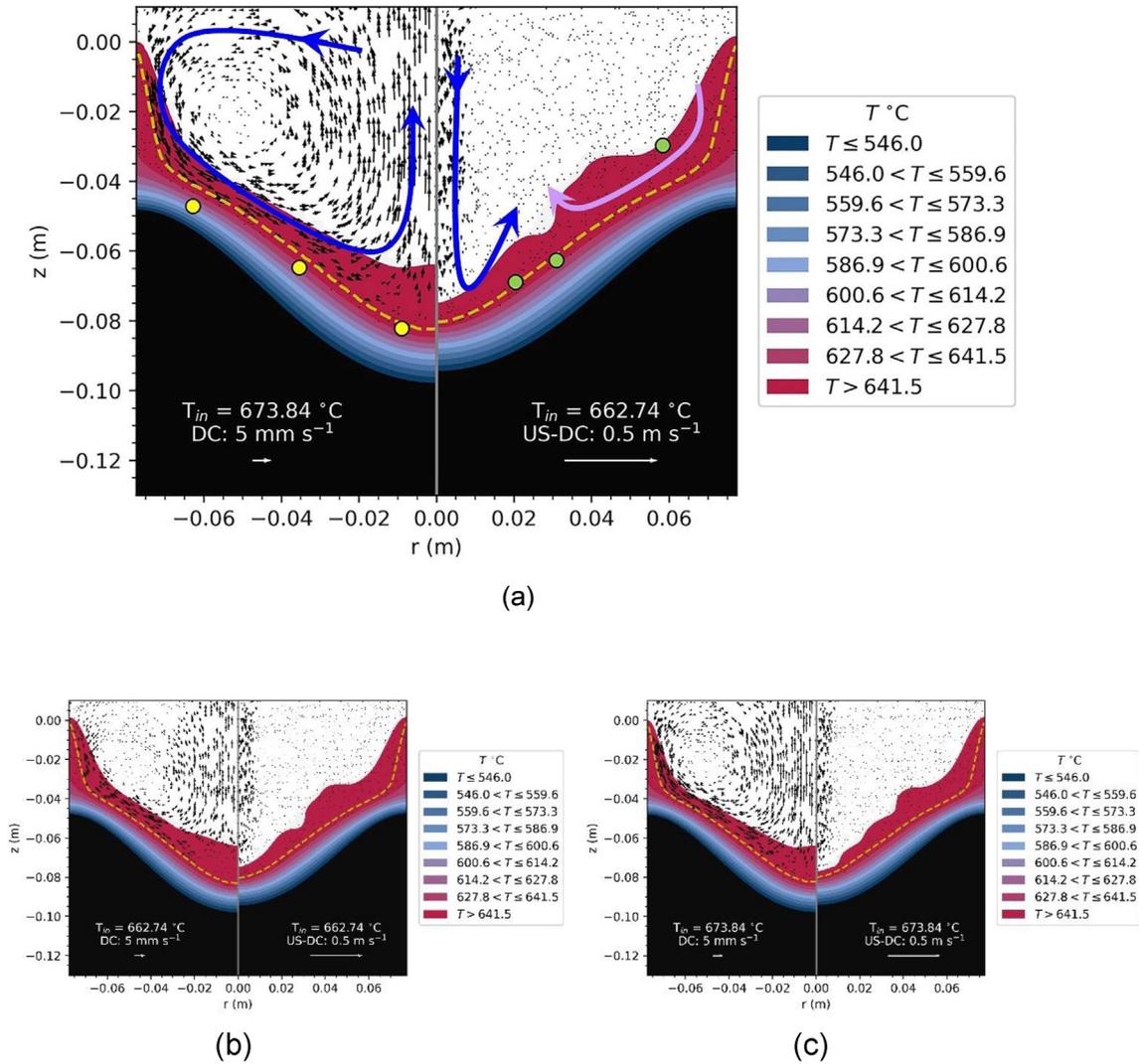
Fig. 8 – (a) Comparison of temperature profile and flow pattern between conventional DC-casting (DC) and UST-DC-casting (US-DC) simulations that have been validated with the temperature measurement results (yellow dots for conventional DC-casting, and green dots for UST-DC casting) at their respective casting temperature; conventional DC-casting, 674 °C, and UST-DC casting case, 663 °C. Comparison of different processes (non-UST − left vs. UST − right) at different cast temperatures; (b) at T = 663 °C and (c) at T = 674 °C. The dashed line in the numerical simulation results represent the isothermal line at $f_s = 0.7$. Arrow lengths depict the magnitude of the flow velocity.

Zn penetration reflects the sump shape satisfactorily down to the border delineating the beginning of a dense mushy zone, thus it does not outline the complete sump geometry.

Multiple-thermocouple recordings during DC casting and results of numerical simulation for both cases (conventional − Fig. 7a and UST-DC casting − Fig. 7b) agree well, especially in the transition temperature range from liquidus (around 655 °C) to solidus (around 533 °C). This is the critical range to simulate casting processes. This good agreement validates the temperature profiles (and ultimately the sump shape) that were generated by the numerical model for both conventional DC-casting and UST-DC-casting processes.

Fig. 8a illustrates that the calculated liquidus isotherm in the UST-DC-casting (right) is more depressed compared with the conventional DC-casting case (left). Overlay between

numerical simulation results and thermocouple position at $f_s = 0.7$ shows that our model predicts the sump shape reasonably well. Temperature measurements (yellow dots for conventional DC casting and green dots for UST-DC casting in Fig. 8a) capture the $f_s = 0.7$ isotherm fairly well. The numerical results also agree with the sump shape reconstructed through thermocouple recordings (Fig. 5). As briefly mentioned previously, this may be explained as the UST-DC casting temperature in the simulations was taken slightly lower (by approx. 10 °C) than in conventional DC-casting, reflecting the measured casting temperature and resulting in a depressed liquidus [56].

In terms of the melt flow pattern, melt flow of the non-UST case depicts the characteristic natural convection flow pattern in DC casting [2,57,58]. Convection is also present in the UST-
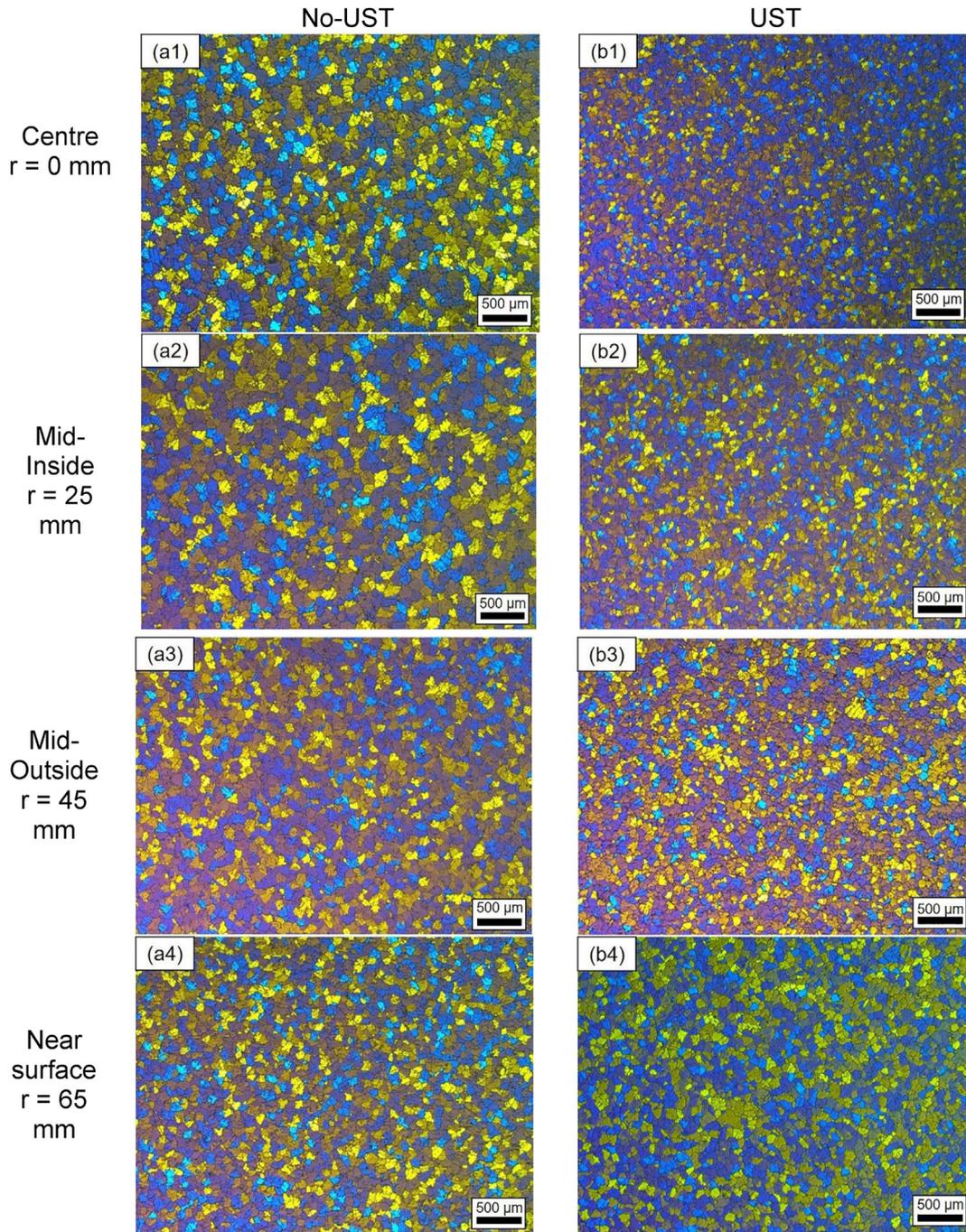
Fig. 9 – Typical anodized grain structure in (a1-a4) conventional DC-casting and (b1-b4) UST-DC-casting. The positions in the billet are shown in the figure.

DC casting (the flow follows light purple arrow on Fig. 8a-right). However, such a flow is opposed and altogether reversed in the center by the acoustic streaming flow (blue arrow on Fig. 8a-right) that has the velocity an order of magnitude higher than the natural convection flow [21,24,25,36–38].

Fig. 8b-c compares different processes (no-UST – left side of the figures, against UST – right side of the figures) at lower casting temperature (Fig. 8b – casting temperature of 663 °C) and higher casting temperature (Fig. 8c – casting temperature of 674 °C). As these figures show, the application of UST significantly depresses the liquid isotherm especially at the center of the billet (below the sonotrode) compared with the non-UST case. Moreover, the increase in casting temperature slightly lowers the liquidus isotherm in both conventional and UST casting. This implies that the higher cooling rate attained in the center of the billet promotes the formation of grains with smaller dendrite arms spacing [38], resulting in better mechanical properties [59]. In addition, a shorter slurry zone is typically linked with reduced macrosegregation [57].

	Center	Mid-In	Mid-Out	Surface
■ Avg. Grain Size - UST	47	61	71	82
■ Avg. Grain Size - No-UST	95	100	86	78
Reduction in Avg. Grain Size (%)	51	39	17	-5
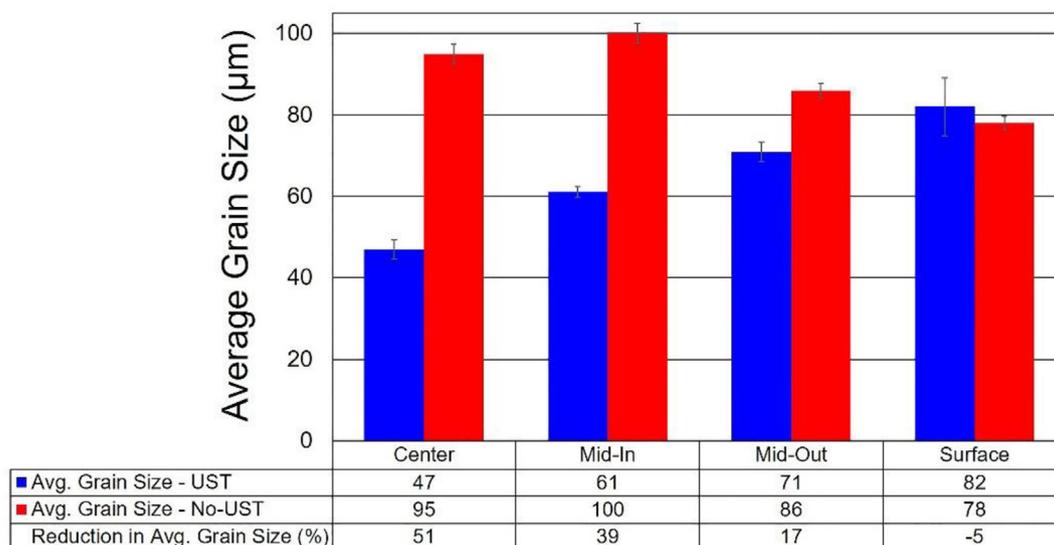
Fig. 10 – Grain size distribution across the billet radius for both conventional DC-casting and UST-DC casting. Mid-in is 25 mm from center, Mid-out is 45 mm from center, and Surface is 65 mm from center. "Reduction" shows the reduction in the average grain size between no-UST and UST billets.

The grain structures shown in Fig. 9 confirm the effectiveness of UST. UST in the hot top refines the grain structure rather significantly (Fig. 9, b1-b4) in contrast with conventional DC casting (Fig. 9, a1-a4). This refinement can be clearly seen especially in the central part of the billet (Fig. 9, b1-b2). Fig. 10 demonstrates that the average grain size in the center of the billet without UST is about 95 μm, while the one cast with UST is approximately 50% finer. The decrease in terms of average grain size from the center to the surface of the billet in the case of conventional DC-casting is around 20%, while the grain size in the case of UST-DC casting almost doubles from the center towards billet surface, almost equaling the conventional DC casting case. The negative value in average grain size reduction in the surface region (shown in Fig. 10) is because the grain is marginally coarser for UST case compared with the conventional DC casting case, though this difference is within a statistical error.

The variation of the average grain size across the billet in the conventional DC casting may be due to the variation of the cooling rate that is largest at the surface of the billet [2]. Meanwhile, the relative increase of the average grain size towards the surface in the UST case is because the area with the most active ultrasonic treatment effect (acoustic streaming and cavitation activities) is below the sonotrode. This cavitation zone in conjunction with acoustic streaming produces a narrower transition zone, increasing number of active substrates and fragmenting the formed dendrites.

The average grain size reduces in the central part of the billet by 50% although the alloy has been already treated with a grain refiner, showing that UST mechanisms work well. Dendrite fragmentation may be the main refinement mechanism in this experimental setting because the largest refinement occurs at the billet center, though deagglomeration and activation of TiB_2 particles from the grain refiner may contribute additionally. Fig. 8 shows how the upper slurry zone is disturbed by the acoustic streaming, resulting in washing up the dendrites, their fragmentation and then return into the transition zone as new grains.

At the same time, the UST-DC cast billet shows a relatively large difference in the grain size across the billet, which may cause a variation in mechanical properties. A simplified estimation from the Hall–Petch relationship (only considering the grain size term) [60] of the yield strength difference between the billet center and its surface gives 25–30%. Such difference is unfavorable for downstream processing. Some of the main UST variables that could be optimized are for instance: distance between sonotrode tip and solidification front and UST power, because these alter the grain structure across the billet [25].

4. Conclusion

Multiple-thermocouple measurements have been carried out during both conventional and UST-DC casting. The recorded temperatures were used to validate numerical predictions of sump profiles. The sump shape has been reconstructed from multiple temperature recordings and overlaying thermocouple positions at certain solid fractions with the temperature profile predicted by the numerical model. The sump was also outlined with a liquid Zn penetration technique. Grain sizes have been measured to assess the effectiveness of UST when the sonotrode is positioned around 20 mm above the graphite ring. The conclusions of this study can be summarized as follows:

1. Quantification of the sump profile with thermocouple measurements is more accurate and less prone to interpretation than with Zn tracing.
2. The numerical model of DC and UST-DC casting has been validated by the temperature measurements across the billets. The experimental results and numerical model are in good agreement.
3. Numerical simulation results show that UST application in the hot top with sonotrode position at 20 mm above the graphite ring level depresses the liquidus isotherm but does not affect the solidus isotherm, resulting in a thinner transition region compared with conventional DC-casting. This promotes the formation of grains with smaller dendrite arms spacing and may reduce the macrosegregation.
4. Acoustic streaming from the sonotrode overcomes the effects of melt inflow from the launder (at rate of 2.5 L min^{-1} corresponding to a casting speed of 140 mm min^{-1}) and assures the symmetry of the sump shape. No asymmetry has been detected in the UST-DC case upon examining two perpendicular billet sections.
5. Grain structure analysis verifies that structure refinement with UST has been achieved at the given sonotrode position. The largest grain refinement was at the center of the billet with the average grain size 50% smaller than that without UST.

Data availability

The data that support the findings of this study are available from the corresponding author upon reasonable request.

Declaration of Competing Interest

The authors declare that they have no known competing financial interests or personal relationships that could have appeared to influence the work reported in this paper.

Acknowledgements

Appendix A Supplementary data

The Supplementary data to this article can be found online at https://doi.org/10.17633/rd.brunel.12974390.

REFERENCES

[1] Granger DA. Ingot casting in the aluminum industry. Treatise Mat Sci Technol 1989;31:109–35. https://doi.org/10.1016/B978-0-12-341831-9.50009-7. Elsevier.

[2] Nadella R, Eskin DG, Du Q, Katgerman L. Macrosegregation in direct-chill casting of aluminium alloys. Prog Mater Sci 2008;53:421–80. https://doi.org/10.1016/j.pmatsci.2007.10.001.

[3] Grandfield JF, Eskin DG, Bainbridge IF. Direct-chill casting of light alloys: science and technology. Hoboken, NJ, USA: John Wiley & Sons, Inc.; 2013. https://doi.org/10.1002/9781118690734.

[4] Stalios A, European Commission. Directorate-General for Research and Innovation. Metallurgy made in and for Europe: the perspective of producers and end-users: roadmap. Luxembourg: Publications Office; 2014.

[5] Quested TE. Understanding mechanisms of grain refinement of aluminium alloys by inoculation. Mater Sci Technol 2004;20:1357–69. https://doi.org/10.1179/026708304225022359.

[6] Murty BS, Kori SA, Chakraborty M. Grain refinement of aluminium and its alloys by heterogeneous nucleation and alloying. Int Mater Rev 2002;47:3–29. https://doi.org/10.1179/095066001225001049.

[7] McCartney DG. Grain refining of aluminium and its alloys using inoculants. Int Mater Rev 1989;34:247–60. https://doi.org/10.1179/imr.1989.34.1.247.

[8] Eskin GI, Eskin DG. Ultrasonic treatment of light alloy melts. 2nd ed. CRC Press; 2015. https://doi.org/10.1201/b17270.

[9] Atamanenko TV, Eskin DG, Sluiter M, Katgerman L. On the mechanism of grain refinement in Al–Zr–Ti alloys. J Alloys Compd 2011;509:57–60. https://doi.org/10.1016/j.jallcom.2010.09.046.

[10] Puga H, Costa S, Barbosa J, Ribeiro S, Prokic M. Influence of ultrasonic melt treatment on microstructure and mechanical properties of AlSi9Cu3 alloy. J Mater Process Technol 2011;211:1729–35. https://doi.org/10.1016/j.jmatprotec.2011.05.012.

[11] Qian M, Ramirez A, Das A. Ultrasonic refinement of magnesium by cavitation: clarifying the role of wall crystals. J Cryst Growth 2009;311:3708–15. https://doi.org/10.1016/j.jcrysgro.2009.04.036.

[12] Ramirez A, Qian M, Davis B, Wilks T, StJohn DH. Potency of high-intensity ultrasonic treatment for grain refinement of magnesium alloys. Scripta Mater 2008;59:19–22. https://doi.org/10.1016/j.scriptamat.2008.02.017.

[13] Tzanakis I, Xu WW, Eskin DG, Lee PD, Kotsovinos N. In situ observation and analysis of ultrasonic capillary effect in molten aluminium. Ultrason Sonochem 2015;27:72–80. https://doi.org/10.1016/j.ultsonch.2015.04.029.

[14] Wang F, Tzanakis I, Eskin D, Mi J, Connolley T. In situ observation of ultrasonic cavitation-induced fragmentation of the primary crystals formed in Al alloys. Ultrason Sonochem 2017;39:66–76. https://doi.org/10.1016/j.ultsonch.2017.03.057.

[15] Priyadarshi A, Khavari M, Subroto T, Conte M, Prentice P, Pericleous K, et al. On the governing fragmentation mechanism of primary intermetallics by induced cavitation. Ultrason Sonochem 2021;70:105260. https://doi.org/10.1016/j.ultsonch.2020.105260.

[16] Shu D, Sun B, Mi J, Grant PS. A high-speed imaging and modeling study of dendrite fragmentation caused by ultrasonic cavitation. Metall Mater Trans 2012;43:3755–66. https://doi.org/10.1007/s11661-012-1188-3.

[17] Tzanakis I, Eskin DG, Georgoulas A, Fytanidis DK. Incubation pit analysis and calculation of the hydrodynamic impact

pressure from the implosion of an acoustic cavitation bubble. Ultrason Sonochem 2014;21:866–78. https://doi.org/10.1016/j.ultsonch.2013.10.003.

[18] Suslick KS, Flannigan DJ. Inside a collapsing bubble: sonoluminescence and the conditions during cavitation. Annu Rev Phys Chem 2008;59:659–83. https://doi.org/10.1146/annurev.physchem.59.032607.093739.

[19] Tzanakis I, Lebon GSB, Eskin DG, Pericleous KA. Characterizing the cavitation development and acoustic spectrum in various liquids. Ultrason Sonochem 2017;34:651–62. https://doi.org/10.1016/j.ultsonch.2016.06.034.

[20] Eskin DG. Ultrasonic processing of molten and solidifying aluminium alloys: overview and outlook. Mater Sci Technol 2017;33:636–45. https://doi.org/10.1080/02670836.2016.1162415.

[21] Lebon B, Tzanakis I, Pericleous K, Eskin D. Numerical modelling of the ultrasonic treatment of aluminium melts: an overview of recent advances. Materials 2019;12:3262. https://doi.org/10.3390/ma12193262.

[22] Jia S, Zhang D, Xuan Y, Nastac L. An experimental and modeling investigation of aluminum-based alloys and nanocomposites processed by ultrasonic cavitation processing. Appl Acoust 2016;103:226–31. https://doi.org/10.1016/j.apacoust.2015.07.016.

[23] Vorozhtsov SA, Eskin DG, Tamayo J, Vorozhtsov AB, Promakhov VV, Averin AA, et al. The application of external fields to the manufacturing of novel dense composite master alloys and aluminum-based nanocomposites. Metall Mater Trans 2015;46:2870–5. https://doi.org/10.1007/s11661-015-2850-3.

[24] Liu Z, Li R, Jiang R, Zhang L, Li X. Scalable ultrasound-assisted casting of ultra-large 2219 Al alloy ingots. Metall Mater Trans A 2019;50:1146–52. https://doi.org/10.1007/s11661-018-5097-y.

[25] Salloum-Abou-Jaoude G, Eskin DG, Lebon GSB, Barbatti C, Jarry P, Jarrett M. Altering the microstructure morphology by ultrasound melt processing during 6XXX aluminium DC-casting. In: Chesonis C, editor. Light met. 2019. Cham: Springer International Publishing; 2019. p. 1605–10. https://doi.org/10.1007/978-3-030-05864-7_203.

[26] Eskin DG, Jafari A, Katgerman L. Contribution of forced centreline convection during direct chill casting of round billets to macrosegregation and structure of binary Al–Cu aluminium alloy. Mater Sci Technol 2011;27:890–6. https://doi.org/10.1179/026708309X12578491814672.

[27] Zhang L, Eskin DG, Miroux A, Subroto T, Katgerman L. Effect of inlet geometry on macrosegregation during the direct chill casting of 7050 alloy billets: experiments and computer modelling. IOP Conf Ser Mater Sci Eng 2012;33:012019. https://doi.org/10.1088/1757-899X/33/1/012019.

[28] Suyitno, Savran VI, Katgerman L, Eskin DG. Effects of alloy composition and casting speed on structure formation and hot tearing during direct-chill casting of Al-Cu alloys. Metall Mater Trans A 2004;35:3551–61. https://doi.org/10.1007/s11661-004-0192-7.

[29] Subroto T, Miroux A, Mortensen D, M'Hamdi M, Eskin DG, Katgerman L. Semi-quantitative predictions of hot tearing and cold cracking in aluminum DC casting using numerical process simulator. IOP Conf Ser Mater Sci Eng 2012;33:012068. https://doi.org/10.1088/1757-899X/33/1/012068.

[30] Lebon GSB, Li H-T, Patel JB, Assadi H, Fan Z. Numerical modelling of melt-conditioned direct-chill casting. Appl Math Model 2020;77:1310–30. https://doi.org/10.1016/j.apm.2019.08.032.

[31] Bennon WD, Incropera FP. A continuum model for momentum, heat and species transport in binary solid-liquid

[32] phase change systems—I. Model formulation. Int J Heat Mass Tran 1987;30:2161–70. https://doi.org/10.1016/0017-9310(87)90094-9.

[32] Tudela I, Sáez V, Esclapez MD, Díez-García MI, Bonete P, González-García J. Simulation of the spatial distribution of the acoustic pressure in sonochemical reactors with numerical methods: A review. Ultrason Sonochem 2014;21:909–19. https://doi.org/10.1016/j.ultsonch.2013.11.012.

[33] Riedel E, Liepe M, Scharf S. Simulation of ultrasonic induced cavitation and acoustic streaming in liquid and solidifying aluminum. Metals 2020;10:476. https://doi.org/10.3390/met10040476.

[34] Nastac L. Mathematical modeling of the solidification structure evolution in the presence of ultrasonic stirring. Metall Mater Trans B 2011;42:1297–305. https://doi.org/10.1007/s11663-011-9539-9.

[35] Jamshidi R, Pohl B, Peuker UA, Brenner G. Numerical investigation of sonochemical reactors considering the effect of inhomogeneous bubble clouds on ultrasonic wave propagation. Chem Eng J 2012;189–190:364–75. https://doi.org/10.1016/j.cej.2012.02.029.

[36] Peng H, Wang Y, Jiang R, Li X, Li R, Zhang L. Numerical simulation of ultrasonic field within the large-scale Al alloy melts treated by scalable sonotrodes. AIP Adv 2019;9:095015. https://doi.org/10.1063/1.5118319.

[37] Komarov S, Yamamoto T. Role of acoustic streaming in formation of unsteady flow in billet sump during ultrasonic DC casting of aluminum alloys. Materials 2019;12:3532. https://doi.org/10.3390/ma12213532.

[38] Lebon GSB, Salloum-Abou-Jaoude G, Eskin D, Tzanakis I, Pericleous K, Jarry P. Numerical modelling of acoustic streaming during the ultrasonic melt treatment of direct-chill (DC) casting. Ultrason Sonochem 2019;54:171–82. https://doi.org/10.1016/j.ultsonch.2019.02.002.

[39] Drezet J-M, Rappaz M, Carrupt B, Plata M. Experimental investigation of thermomechanical effects during direct chill and electromagnetic casting of aluminum alloys. Metall Mater Trans B 1995;26:821–9. https://doi.org/10.1007/BF02651729.

[40] Eskin DG, Zuidema J, Savran VI, Katgerman L. Structure formation and macrosegregation under different process conditions during DC casting. Mater Sci Eng A 2004;384:232–44. https://doi.org/10.1016/j.msea.2004.05.066.

[41] Yu KC, Guo SJ, Nagaumi H. Evaluation on the accuracies of sump depth measurements during DC casting process of 7050 alloy. Mater Sci Forum 2016;877:78–83. https://doi.org/10.4028/www.scientific.net/MSF.877.78.

[42] Andersson J-O, Helander T, Höglund L, Shi P, Sundman B. Thermo-Calc & DICTRA, computational tools for materials science. Calphad 2002;26:273–312. https://doi.org/10.1016/S0364-5916(02)00037-8.

[43] Louisnard O. A viable method to predict acoustic streaming in presence of cavitation. Ultrason Sonochem 2017;35:518–24. https://doi.org/10.1016/j.ultsonch.2016.09.013.

[44] Trujillo FJ. A strict formulation of a nonlinear Helmholtz equation for the propagation of sound in bubbly liquids. Part I: Theory and validation at low acoustic pressure amplitudes. Ultrason Sonochem 2018;47:75–98. https://doi.org/10.1016/j.ultsonch.2018.04.014.

[45] Jamshidi R, Brenner G. Dissipation of ultrasonic wave propagation in bubbly liquids considering the effect of compressibility to the first order of acoustical Mach number. Ultrasonics 2013;53:842–8. https://doi.org/10.1016/j.ultras.2012.12.004.

[46] Gadi Man YA, Trujillo FJ. A new pressure formulation for gas-compressibility dampening in bubble dynamics models.

Ultrason Sonochem 2016;32:247—57. https://doi.org/10.1016/j.ultsonch.2016.03.013.

[47] Toegel R, Gompf B, Pecha R, Lohse D. Does water vapor prevent upscaling sonoluminescence? Phys Rev Lett 2000;85:3165—8. https://doi.org/10.1103/PhysRevLett.85.3165.

[48] Voller VR, Prakash C. A fixed grid numerical modelling methodology for convection-diffusion mushy region phase-change problems. Int J Heat Mass Tran 1987;30:1709—19. https://doi.org/10.1016/0017-9310(87)90317-6.

[49] Vreeman CJ, Krane MJM, Incropera FP. The effect of free-floating dendrites and convection on macrosegregation in direct chill cast aluminum alloys: Part I: model development. Int J Heat Mass Tran 2000;43:677—86. https://doi.org/10.1016/S0017-9310(99)00174-X.

[50] Lebon GSB, Tzanakis I, Djambazov G, Pericleous K, Eskin DG. Numerical modelling of ultrasonic waves in a bubbly Newtonian liquid using a high-order acoustic cavitation model. Ultrason Sonochem 2017;37:660—8. https://doi.org/10.1016/j.ultsonch.2017.02.031.

[51] Stefanescu DM. Science and engineering of casting solidification. Cham: Springer; 2015.

[52] Menter FR, Kuntz M, Langtry R. Ten years of industrial experience with the SST turbulence model. Turbul Heat

mass transf, vol. 4. Antalya, Turkey: Begell House; 2003. p. 625—32.

[53] Weller HG. OpenFOAM. OpenCFD Ltd (ESI Group); 2018.

[54] Rohsenow WM, Hartnett JP, Cho YI. Handbook of heat transfer. 3rd ed. New York: McGraw-Hill; 1998.

[55] Menter FR, Esch T. Elements of industrial heat transfer predictions. 16th Braizlian Congr. Mech Eng COBEM 2001;109.

[56] Eskin DG, Savran VI, Katgerman L. Effects of melt temperature and casting speed on the structure and defect formation during direct-chill casting of an Al-Cu alloy. Metall Mater Trans A 2005;36:1965—76. https://doi.org/10.1007/s11661-005-0059-6.

[57] Eskin DG. Physical metallurgy of direct chill casting of aluminum alloys. Boca Raton: CRC Press/Taylor & Francis; 2008.

[58] Du Q, Eskin DG, Katgerman L. The effect of ramping casting speed and casting temperature on temperature distribution and melt flow patterns in the sump of a DC cast billet. Mater Sci Eng A 2005;413—414:144—50. https://doi.org/10.1016/j.msea.2005.08.176.

[59] Radhakrishna K, Seshan S. Dendrite arm spacing and mechanical properties of aluminium alloy castings. Cast Met 1989;2:34—8. https://doi.org/10.1080/09534962.1989.11818980.

[60] Dieter GE, Bacon D. Mechanical metallurgy. SI metric ed. London: McGraw-Hill; 2001.